Time of Flight Diffraction for rough planar defects

Stewart G Haslinger[a,b], Michael J S Lowe[b], Zhengjun Wang[c] and Fan Shi [c,*]

[a]*Department of Mathematical Sciences, University of Liverpool*

[b]*Department of Mechanical Engineering, Imperial College, London*

[c]*Department of Mechanical and Aerospace Engineering, Hong Kong University of Science and Technology*

A B S T R A C T

Ultrasonic non-destructive evaluation techniques, such as time-of-flight diffraction (ToFD) for which the arrival times of waves diffracted from crack tips are analysed to locate and size defects, are well understood for smooth defects. In environments where extreme changes in temperature and pressure occur, the damage that may arise is often non-uniform and more difficult to characterise when designing and qualifying an inspection. This article investigates the implementation of ToFD methods for sizing rough defects using a purely theoretical approach. High-fidelity finite element modelling and stochastic Monte Carlo methods are used to provide physical and statistical insights for the dependence on both incident beam angle and degree of roughness for the case of planar defects. Optimal incident angles for ultrasonic ToFD techniques were determined in the 1980s but largely based on theoretical and experimental investigations for smooth defects. However, rough defects produce tip-diffracted signatures that are more complicated than for their smooth counterparts, largely due to multiple scattering effects related to mode conversion and propagation of surface waves along the rough surface. It is shown that roughness may cause larger diffraction amplitude values at different angles, which leads to increased uncertainty when sizing, with illustrative examples and physical interpretations provided. Comparisons of amplitudes for smooth and rough defects of the same size are also demonstrated. The ToFD method, using envelope peak detection and autocorrelation approaches, is implemented to estimate the size of rough cracks, and the effects of roughness on the accuracy of this sizing are investigated with statistical analysis.

1. Introduction

The scattering of elastic waves in solids is well known to be affected by surface roughness [1]. No two rough surfaces are the same, meaning that a rough defect can be modelled as a randomly generated dataset. Examples include thermal fatigue or stress corrosion cracks, which may arise when a nuclear power plant component is subjected

5   to extreme changes in temperature and pressure. The prediction of expected amplitudes when ultrasound is reflected from the surface of a rough defect has been studied extensively using statistical techniques for application within non-destructive evaluation (NDE) techniques.

Crucial work in the UK was carried out by Ogilvy and colleagues [2], [3], [4] in the 1980s, whereby the reflected signal from a rough surface was calculated using the Kirchhoff approximation (KA) [5]. Improved finite element

---

*Corresponding author

✉ maefanshi@ust.hk (F.S.)

ORCID(s):

[10] modelling capability [6] and scattering matrix methods [7, 8] brought further advances. The recent series of papers by Shi *et al.* [9, 10, 11] advocates a stationary phase approximation of the reflection using KA (termed SPARK by [12]) to predict the expected amplitude without specific knowledge of the geometry of a defect. These recent advances indicate that the predictions of the model derived by [2] may be over-conservative in some situations by as much as 20dB [12].

[15] The modelling of rough surface reflection of ultrasound is directly relevant for technical justifications associated with the qualification of an inspection procedure that incorporates pulse-echo (P-E) and pitch-catch set-ups, to improve the detectability of a rough crack. It is also important to size a crack after detection, since the length [1] provides critical information regarding the structural integrity of the component. The ultrasonic ToFD approach [13], which relies on the elastic wave diffracted from defect tips or edges, is widely used for defect sizing. A pair of transmitting and [20] receiving transducers measures the times of arrival of waves diffracted from the tips of a defect to determine its size in the through-thickness direction. A schematic illustration (taken from the British Standard implementation of EN ISO 16828:2014 [13]) is shown in Figure 1.
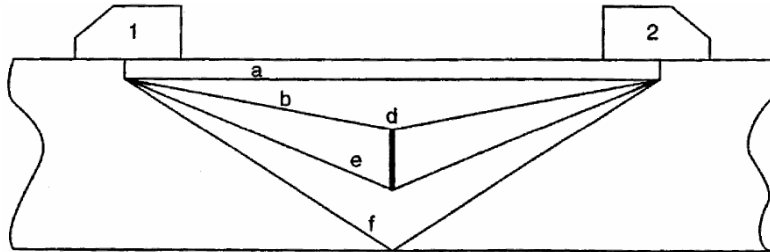
Figure 1: Schematic illustration of ToFD technique (taken from [13]). A smooth embedded defect is shown with the transmitter and receiver labelled as 1 and 2, respectively. Wave paths *a* and *f* represent the lateral wave and backwall echo, respectively. The top tip is *d* and the ray paths for the upper and lower tip signals are denoted by *b* and *e*.

The insonification of the defect in Figure 1 by an ultrasonic wave emitted from the transmitter (labelled 1) results in three general processes: surface reflections, excitation and propagation of Rayleigh waves along the defect surfaces [25] and the diffraction of spherical or cylindrical waves (or circular in two-dimensional space) from the crack tips, which are collected by the receiver 2 in Figure 1. Mode conversions from compression (P) to shear (S) waves, and vice versa, occur and must be taken into account for both bulk and surface waves associated with the defect. The sizing of a

---

[1]In this two-dimensional study, length is used to denote the vertical dimension of the crack as shown in Figure 1. However, we acknowledge that in three-dimensional practice, this dimension is often referred to as width and the dimension out of the page is referred to as crack length.

smooth embedded defect is estimated by measuring the difference in times of arrival of waves scattered from the top (or upper) and bottom (or lower) tips and then applying elementary geometrical considerations. Although amplitude information is not used explicitly in these calculations, it is an important factor to optimize the ultrasonic beam angle since tip diffracted signals are often at least two orders of magnitude lower than specular reflections.

The paper by Ogilvy & Temple [14] provides theoretical calculations for the angular distribution of tip diffraction amplitude for an infinite monochromatic wave incident on an isolated crack tip. The equations for the theoretical scattering amplitudes are derived from the mathematical model developed by Chapman [15], based on the geometrical theory of diffraction (GTD) introduced for the field of optics by Keller [16]. In the early 1950s, the problem was solved for a semi-infinite crack by Maue [17] with results that are consistent with [14, 15]. Achenbach and co-workers have contributed numerous works on the scattering of ultrasound by elastic cracks with much of the research summarised by Achenbach *et al.* [18] in a book on ray methods for wave scattering by cracks in elastic solids. As noted by Phillips [19], much of the theoretical work is based on several limiting assumptions, including a far field assumption, high frequency approximation and that the defect is smooth, flat and semi-infinite. Relatively little attention has been given to the case of finite rough planar defects, which is the focus of the work here. As will be seen later, roughness significantly affects the amplitude, and distorts the waveforms, of the tip diffractions.

The authors of [14] mentioned the role of roughness but only regarding the limiting assumption related to the face-to-face separation gape of a defect and the wavelength of the incident elastic wave. A recent article [20] considered the case of near-backwall surface-breaking defects within thick section components, including an investigation of the effect of roughness for angled beam P-E inspection. Surface roughness of a crack is known to affect sizing techniques that rely on time-differences of signals diffracted from defect extremities [21]. In particular, [22] provides an illustrative example for angled P-E inspection for which a continuous pulse is obtained for a rough defect such that the diffracted signals from the tips of the defect are not distinct. Instead, the signal consists of a superposition of edge-diffracted waves and diffuse scattering from the whole surface of the flaw.

The work by Zhang *et al.* [8] investigated how roughness affects the sizing of small defects (of around two wave-lengths in length) when implementing the total focusing method (TFM) imaging algorithm. It was found that roughness can be beneficial or detrimental to the detectability of a crack-like defect and that it often causes underestimation of the crack length. A subsequent article by Elliott *et al.* [23] considered the use of super-resolution (SR) algorithms (the

factorization (FM) and time reversal multiple-signal classification (TR-MUSIC) methods) to investigate scattering data for small (sub-wavelength) rough embedded planar defects. It was shown that both the FM and TR-MUSIC algorithms were able to size, and estimate defect orientation, accurately for roughness up to 100μm. The data were acquired using full matrix capture, and the FM and TR-MUSIC techniques were applied over multiple frequencies. A comprehensive comparison was also provided by [23], with the sizing capability of the SR algorithms shown to be significantly better than TFM for sub-wavelength defects.

The present article considers only the ToFD method (thereby ruling out surface reflections in general) for a vertical crack such that a single A-scan trace provides sufficient information for sizing a smooth crack, with prior knowledge of its location. High-fidelity finite element (FE) and Monte Carlo (MC) methods are implemented to take account of complex defect morphologies and geometries for the case of finite embedded defects, for which the ultrasound is diffracted by both crack tips. The introduction of roughness and variation in the incident beam angle leads to A-scans consisting of continuous signals for which sizing becomes problematic. A comparison of the diffracted signals from a smooth and rough crack (of the same size and simulated using FE methods) is shown in Figure 2 for beam angles of (a) 70° and (b) 30°.

(a) 70° beam angle. (b) 30° beam angle.
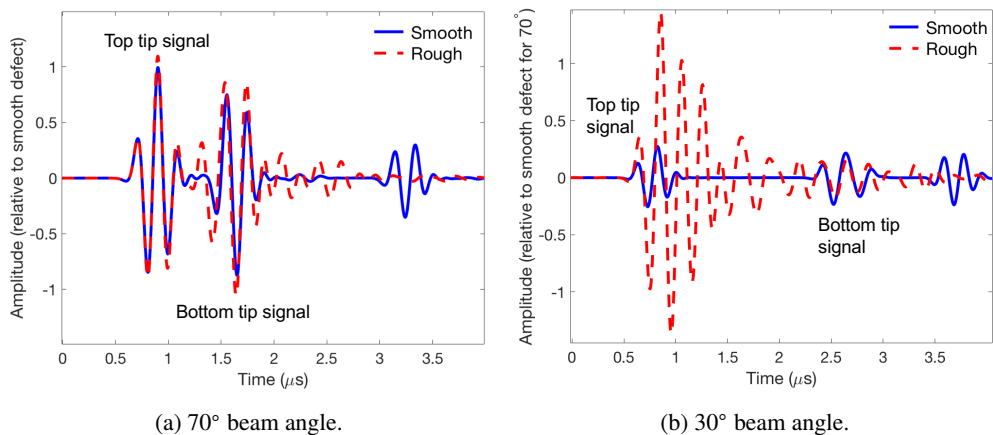
Figure 2: Effect of roughness on tip diffracted signals for a ToFD inspection. A smooth and rough defect, each of length 6mm and at depth 30mm, are insonified by a 5MHz 3-cycle compression wave (for stainless steel material parameters, $c_p = 5940\text{ms}^{-1}$, $c_s = 3230\text{ms}^{-1}$). The rightmost signals in both figures represent multiple scattering signals explained in detail in Section 2.3. Back-wall echoes are absent due to the inclusion of absorbing layers in the FE model.

Figure 2 shows signals for a ToFD set-up with the transmitter and receiver located symmetrically about a vertically aligned defect of open type (as illustrated in the schematic Figure 1). Compression waves with a centre frequency of 5MHz, and a 3-cycle excitation, insonify the smooth (solid blue) and rough (dashed red) defects which are embedded

within a two-dimensional, isotropic, stainless steel specimen with the compression wave speed $c_p = 5940\text{ms}^{-1}$ and shear wave speed $c_s = 3230\text{ms}^{-1}$. The resultant A-scans indicate that both beam angles produce distinct diffracted signals for the smooth defect but only the beam angle of 70° in Figure 2(a) produces two distinct diffracted signals for the rough defect. In contrast, the choice of 30° in Figure 2(b) produces a superposition of several waves that make sizing challenging, and the amplitude for the top tip is much larger than for 70°. The focus of this article is to investigate how both the degree of roughness and the incident beam angle affect the implementation of ToFD techniques with respect to amplitudes and sizing for rough defects.

The article is organised as follows: Section 2 reviews the theoretical method developed by Chapman for ultrasonic ToFD inspections of smooth defects and comparisons are made with FE results for finite-sized defects, the models of which are implemented for rough defects for the rest of the paper. Section 3 provides analysis of the effect of roughness on the amplitudes of the tip-diffracted signals for rough defects, with a focus on preferred beam angles. Section 4 explores how changing the beam angle influences the received signals, with physical explanations of the wave scattering phenomena observed. Section 5 reviews the sizing capability of ToFD for rough defects, using both peak-to-peak and autocorrelation methods. Error bounds are also provided. Concluding remarks and the future outlook for the work are drawn together in Section 6.

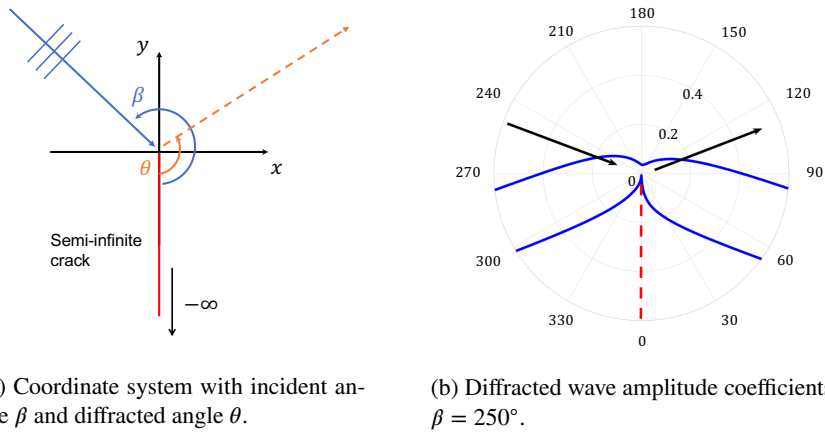## 2. Modelling of tip-diffracted waves for smooth cracks

An ultrasonic wave undergoes diffraction when encountering the tip or edge of a crack within an elastic solid. For the case of a tapered point, spherical waves are generated (circular waves in a two-dimensional plane) and for an edge, cylindrical waves are generated. Mode conversion also occurs, with the transfer of energy between S and P bulk waves, and the generation of surface waves upon insonification of the defect. In this paper, we specialise to two-dimensional space and P-wave incidence for all of the examples and results; similar studies may be performed for S-wave incidence.

2.1. Theoretical model for diffracted amplitudes for a semi-infinite smooth crack

In the 1980s, with the advent of the ultrasonic ToFD inspection technique for NDE, a theoretical mathematical model was developed by Chapman [15] to predict the amplitudes for the diffraction of elastic waves by a semi-infinite crack. The results are summarised in [14] together with the statement of the problem and fundamental assumptions.

The model is based on the geometrical theory of diffraction (GTD) that was published by Keller [16] for the field of optics in the 1960s. Important assumptions are that the crack is open (each face acts independently of one another) and that the spacing or gape s between defects faces is significantly smaller than the incident wavelength λ, and greater than the displacement amplitude δ. For typical NDE frequencies of a few MHz up to 10MHz, wavelengths vary from around one half to a few millimetres for steel. Typical values for δ are of the order of nanometres [14].

The coordinate system is shown in Figure 3, where the crack extends to $y = -\infty$, and to $z = \pm\infty$ in the z-direction (out of the plane of the page) and plane strain is assumed. Note that the coordinate system in Figure 3 differs from that given in [14], since the orientation of the semi-infinite crack tip has been aligned with the top tip of the ToFD set-up for the finite rough defects considered subsequently.

(a) Coordinate system with incident angle β and diffracted angle θ.

(b) Diffracted wave amplitude coefficients for $\beta = 250°$.

Figure 3: Diffraction of incident P-wave by a semi-infinite crack (red). In part (b), largest amplitudes (indicated by distance from the origin in the polar plot) are for the specular reflected direction ($\theta = 290°$) and the straight-through signal ($\theta = 70°$); the diffracted wave is shown by the black arrow.

The angle of incidence β is shown in Figure 3a; the diffracted wave direction is denoted by the dashed line and has an angle of θ. Following the method of Chapman cited by [14], the diffracted wave potentials for smooth cracks and incident compression waves may be expressed in the forms:

$$\phi_d = G_p(\theta, \beta)\left(\frac{\lambda_p}{R}\right)^{1/2} e^{ik_p R}; \qquad \psi_d = G_s(\theta, \beta)\left(\frac{\lambda_s}{R}\right)^{1/2} e^{ik_s R}, \tag{1}$$

for diffracted P and S waves, respectively, where R is the distance from the crack tip to the receiver. The compression and shear wavelengths are represented by λ_p and λ_s, respectively, and the wave numbers for the P and S waves are denoted by k_p, k_s. As mentioned earlier, mode conversion to Rayleigh surface waves also occurs, and the corresponding

wave number is given by k_R in what follows.

This article investigates the P-P case for rough defects, so only the G_p expression is provided explicitly here but all diffraction amplitude expressions are provided by [14]:

$$G_p(\theta, \beta) = e^{i\pi/4} \frac{k_p^2 \sin\frac{\beta}{2}\left[\sin\frac{\theta}{2}(\cos^2\beta - \kappa^2)(\cos^2\theta - \kappa^2) + k_p \cos\frac{\beta}{2}\cos\beta\sin 2\theta \sqrt{(k_s - k_p\cos\theta)(k_s - k_p\cos\beta)}\right]}{\pi(k_s^2 - k_p^2)(\cos\theta + \cos\beta)(k_R - k_p\cos\theta)(k_R - k_p\cos\beta)K^+(-k_p\cos\theta)K^+(-k_p\cos\beta)}, \quad (2)$$

where $\kappa = k_s/k_p$ and the function $K^+(\alpha)$ is defined as follows:

$$K^+(\alpha)K^-(\alpha) = K(\alpha) = \frac{4\alpha^2(\alpha^2 - k_p^2)^{\frac{1}{2}}(\alpha^2 - k_s^2)^{\frac{1}{2}} - (2\alpha^2 - k_s^2)^2}{2(k_s^2 - k_p^2)(\alpha^2 - k_R^2)}, \quad (3)$$

$$K^\pm(\alpha) = \exp\left[\frac{-1}{\pi}\int_{k_p}^{k_s}\arctan\left(\frac{4x^2(x^2 - k_p^2)^{\frac{1}{2}}(k_s^2 - x^2)^{\frac{1}{2}}}{(2x^2 - k_s^2)^2}\right)\frac{dx}{x \pm \alpha}\right], \quad (4)$$

which are derived using the Wiener-Hopf technique, with details provided by, for instance, Achenbach [18, 24].

The expressions for the diffracted wave amplitudes are valid in the far field limit, i.e. $k_p R \gg 1$ and $k_s R \gg 1$, and various illustrative examples for NDE applications were shown in [14]. For NDE applications, where crack-like defects normal to the surface are, together with surface-breaking cracks, among the most important to detect, it is very useful to identify the optimal incident beam angles for the case of a symmetrically placed defect. In this scenario, the signal at the receiver depends only on a single angle γ, defined between the incident beam and the $y-$axis in Figure 4a, since the diffracted angle will take the same value due to the symmetry.

The work of [14] identified the optimal angle, for an embedded defect, to be $\gamma \simeq 70°$ for P-wave incidence, with different angular ranges identified for both P-wave and S-wave incidence for surface-breaking defects. A polar plot of the diffraction coefficients for P-waves is shown here in Figure 3b. It is clear that the amplitudes of the straight-through and specularly reflected signals are much greater than in the diffracted direction, but in most scenarios, the diffracted amplitudes are sufficiently large to be detectable. However, it should be noted that in practice, the capability for detecting diffraction signals is dependent on the threshold and noise levels. With the inclusion of range-dependence R, $\gamma = 70°$ (or equivalently $\beta = 250°$) is an optimal beam angle for symmetrically placed finite embedded defects.

¹³⁰ ## 2.2. Finite element model for symmetrically placed defects

In order to demonstrate the reliability of the FE models used within the MC analysis for randomly rough defects, initial cases for smooth defects were compared and validated with the predictions from the Chapman theoretical model. In this section, the underlying FE model is introduced and explained for the case of a finite-sized smooth embedded defect, of length 6mm and maximum gape $s = 0.15$mm. For increased values of γ, the dimensions of the models

¹³⁵ grow such that the implementation of a three-dimensional model would incur a significant computational burden in the context of a MC analysis of the effect of roughness. This article considers only the 2D diffraction model, but the same approach may be extended to the 3D case.

The fundamental FE domain is shown in Figure 4a for the case of a symmetrically placed defect, relative to the transmitter and receiver. As mentioned previously, stainless steel material parameters were implemented: $c_{\mathrm{p}} = 5940$ms^{-1},

¹⁴⁰ $c_{\mathrm{s}} = 3230$ms^{-1}. In the ToFD simulation, the top tip depth $d = 30$mm is fixed and γ is varied from 15° to 82°. The depth of 30mm was chosen as a representative value of interest to industry (private communication with EDF Energy UK) but the model is easily adaptable to alternative crack depths and through-wall thicknesses. Similarly, all results here are for a typical NDE centre frequency of 5MHz (for P-wave incidence), but the model supports universal frequency analysis.
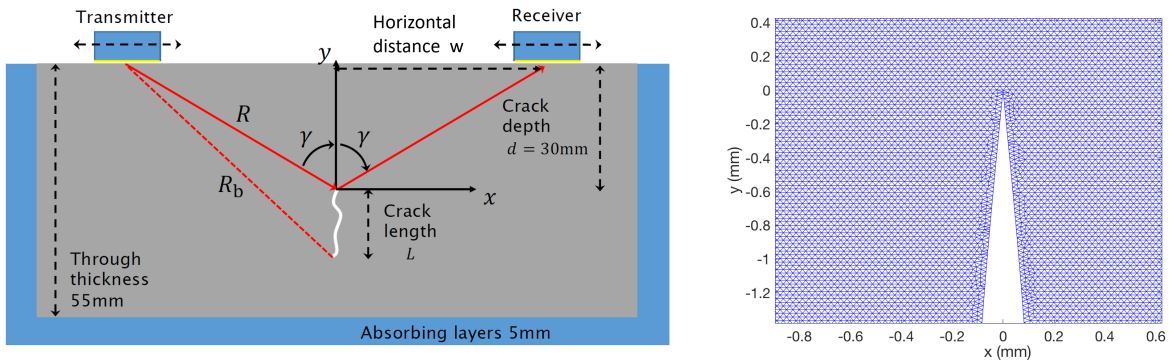
(a) Incident beam angle is denoted by γ, $R(R_{\mathrm{b}})$ is the distance from top (bottom) tip to transmitter/receiver.

(b) Magnification of the triangular meshing elements for a 6mm smooth defect.

Figure 4: FE model for ToFD simulation for a symmetrically placed defect, with the top tip fixed at 30mm depth. The defect may be rough or smooth and has length L.

¹⁴⁵ The dimensions of the FE domain vary with γ to maintain the fixed top tip depth of $d = 30$mm, such that the lateral separation of the source and receiver $2w = 2d \tan \gamma$. There is also an additional 10mm on the left and right

to allow for the inclusion of absorbing layers to remove unwanted reflections (5mm, $\simeq 4.2\lambda_{\mathrm{p}}, 7.7\lambda_{\mathrm{s}}$) and to ensure that the source and receiving nodes are located outside of these absorbing boundaries. Therefore the dimensions vary from 36mm×60mm to 450mm×60 mm, for which the number of elements exceeds 100 million. The mesh size is $\Delta x = 25\mu$m, which corresponds to roughly $\lambda_{\mathrm{p}}/50$ and $\lambda_{\mathrm{s}}/25$.

Plain strain 3-noded linear triangular elements (CPE3) were used in the high-fidelity GPU-based software package Pogo [25], which incorporates its own meshing tool. Figure 4(b) illustrates the mesh around the tip of a smooth defect, where the pogoMesh function generates an irregular mesh in the immediate vicinity but reverts to a regular form in a highly efficient way as the distance from the defect increases. Pogo is an explicit time domain FE solver for elastic waves, and all the computations in this article were performed using a single Nvidia GTX 1080Ti GPU card, with 11GB of memory. The run-time for the smallest models was less than 1 minute, and for the largest models, with > 100 million degrees of freedom (DOF), less than 10 minutes.

The underlying excitation is a 3-cycle Hann-windowed toneburst (investigations were also conducted for a 2-cycle toneburst) with a centre frequency of 5MHz. This excitation was applied to a 10mm source line, with the appropriate time delay applied to each excitation node. A spatial Gaussian windowing function was also implemented to generate a tapered plane wave, with a beam width of around 5mm, at the given angle γ; details were described in [10, 26]. The length of the receiving nodes was set to be the same as that of the source nodes, i.e. 10mm. The centres of the source and receiving lines are positioned a distance R (which is calculated as $d/\cos\gamma$) from the top tip of the defect. For each angle of incidence simulated, a corresponding control simulation (with no defect but identical excitation and FE domain) was performed, from which the scattered signal was obtained by evaluating the difference between two signals. The time step was defined by setting the Courant number to 0.3 and a total simulation time of 40μs led to 31,679 time steps, following the guidance of [27].

Following the original results of [14], the diffracted amplitudes G_{p} in equation (2) are used to plot the received signal amplitudes, normalised with respect to the amplitude at the top tip of the defect and propagated to the receiver, for the set-up illustrated in Figure 4. The comparison is made with the FE results, for which the post-processing was performed in both the time and frequency domains. Windowing was applied to the tip-normalised diffracted scattered signal, followed by zero padding and then application of a Hilbert envelope in the time domain, or a fast Fourier transform to obtain the frequency domain result. In Figure 5, the latter method was applied and the centre frequency

component (5MHz) is taken for comparison with the theoretical model.
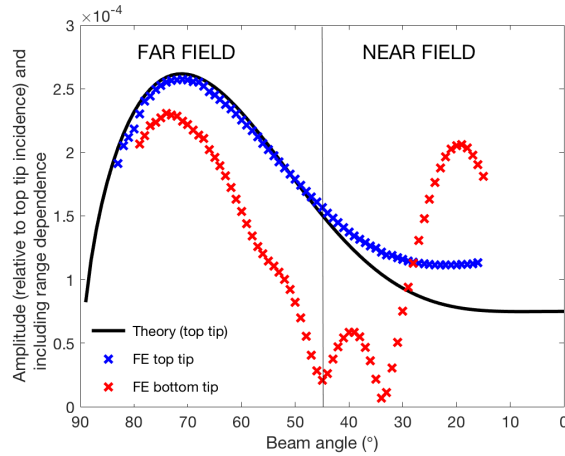
Figure 5: Comparison of theoretical and FE results for range of beam angles $15° \leq \gamma \leq 82°$ for a smooth 6mm embedded planar defect. The amplitude is normalised relative to the signal at the tip, and R-dependence (top tip of the defect was located at a depth of 30mm) is included.

The comparison shows very good agreement, particularly over the range $45° \leq \gamma \leq 80°$. For the lower values of γ, $45° \geq \gamma \geq 15°$, the distance R decreases to the range $42\text{mm} \geq R \geq 31\text{mm}$. Recalling that the theoretical model incorporates a far field approximation and a semi-infinite crack, it is notable in Figure 5 that for $\gamma < 45°$, the theoretical predictions (solid black line) start to deviate from the FE results (indicated by the blue '×'). This appears to be due to the transition from the far field to the near field and the finite size of the defect.

The FE results for the bottom tip (normalised with respect to the amplitude of the signal at the top tip, and including the dependence on R_b) are shown by the red markers '×' in Figure 5, and give an idea of the variation of amplitudes between the top and bottom tips for the set-up shown in Figure 4(a). It is clear that for a smooth defect, a beam angle of around $\gamma = 70°$ facilitates detection of both the top and bottom tip signals, since they share similar elevated amplitude values at these angles.

2.3. Secondary scattering effects for smooth defects

As mentioned in Section 1, Figure 2(a) illustrates the key concept of the ToFD sizing technique, namely to determine the difference in times of arrival of top and bottom tip signals. Figure 6(a) features the same A-scans as Figure 2(a), but with additional annotations to highlight another fundamental feature that is useful to identify a smooth defect. The third peak for the smooth defect, that initiates at around 3μs and is labelled as Surface-bulk in Figure 6(a),

is the result of a secondary scattering process in which a surface wave (initially excited when the incident bulk wave arrives at the top tip) has propagated along the surface of the defect and then converts to a diffracted bulk wave at the bottom tip. This is easily verified by some simple calculations with the material wave speeds c_p and c_R, distances involved and that for the transmitter in the far field, the incident waves arriving at the crack may be considered as plane waves. The FE model is designed such that the beam angle γ is directed towards the top tip. The far field assumption then implies that the incident angles for both tips are equal to γ.

(a) Times of arrival T_1, T_2, T_3. (b) Ray paths for the first 3 arrivals.
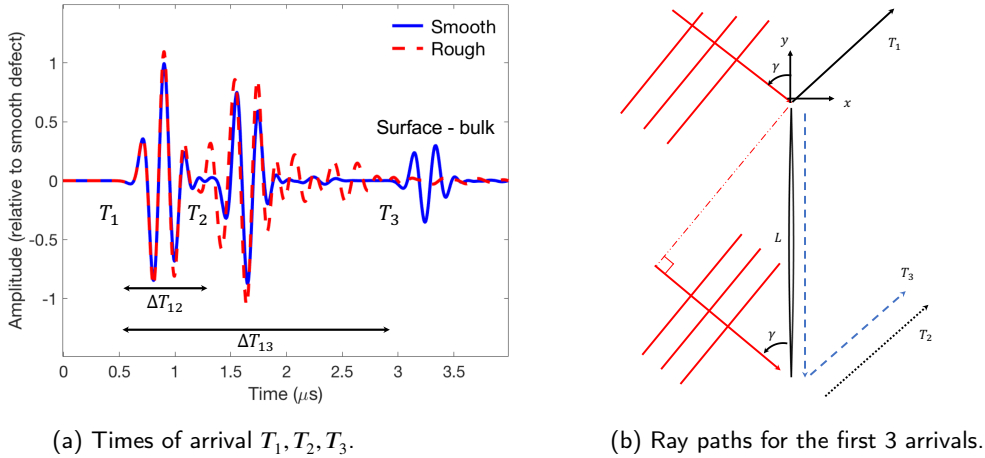
Figure 6: Scattering mechanisms for a 6mm smooth defect. The A-scan for the smooth defect in part (a) shows an additional peak at T_3 which denotes the time of arrival for the received signal marked by the dashed blue arrow in part (b).

Denoting the times of arrival as T_1, T_2 and T_3, as labelled in Figure 6(a), the differences may be calculated using the ray paths illustrated in the schematic Figure 6(b), where the arrows indicate the beam paths for top tip (T_1), bottom tip (T_2) and top tip-surface wave-bottom tip (T_3). The time differences for the top and bottom tip, and top and surface-bulk signal, are denoted by ΔT_{12} and ΔT_{13}, respectively.

Taking the wave speeds as outlined in Section 2.2: $c_p = 5940\text{ms}^{-1}, c_s = 3230\text{ms}^{-1}$ and the Rayleigh wave speed $c_R = 2986\text{ms}^{-1}$ via the Rayleigh wave equation given by Achenbach [24], the time differences ΔT_{12} and ΔT_{13} for $\gamma = 70°$ are calculated as follows:

$$\Delta T_{12} = 2\frac{L\cos\gamma}{c_p} = 0.69\mu s; \qquad \Delta T_{13} = \frac{L\cos\gamma}{c_p} + \frac{L}{c_R} = 2.35\mu s. \qquad (5)$$

Comparison of these estimated time differences and the signals in Figure 6(a) verify the scattering mechanisms that give rise to the individual waveforms. It should also be noted that the third waveform not only represents the top

tip-surface wave-bottom tip scenario, but also includes some contribution from a bottom tip-surface wave travelling upwards-top tip mechanism, since the time windows involved are identical.

An additional point of interest from the smooth-rough defect comparison in Figure 6(a), is the change of phase associated with diffraction from a top or bottom tip. As first mentioned by [14], for incident and diffracted P waves, there is always a phase difference of π between top and bottom tip signals, and this is demonstrated by the waveforms marked as T_1 and T_2 in Figure 6(a). With reference to Figure 6(b), and the semi-infinite assumption in Figure 3, it can be observed that for the bottom tip, the finite defect is effectively flipped through π to give a corresponding incident angle of $-\pi + \gamma$ leading to the phase change of π demonstrated by the top and bottom tip signals in Figures 2(a) and 6(a).

This characteristic phase change is very useful when sizing a smooth defect, since it is a clear diagnostic feature. It follows that it is also potentially useful for sizing rough defects, as for the case of $\gamma = 70°$ and the specific realisation featured in Figure 2(a). However for higher degrees of roughness and alternative beam angles, as in Figure 2(b), the signal may become so convoluted that it is no longer straightforward to characterise a signal in this way. The signal for the case of $\gamma = 30°$ no longer demonstrates a clear top-bottom tip phase change and this is due to numerous scattering events that follow consecutively between the arrival of the incident beam at the top tip, and when it has been scattered by the bottom tip.

3. Effect of roughness on amplitudes

The roughness of a surface is typically characterized by two statistical parameters [1], the standard deviation σ, or root mean square (RMS) value, of height relative to a reference surface, and the lateral correlation length λ_0, which determines the statistical independence of a rough surface's peaks and troughs. The RMS height may be defined formally as:

$$\sigma = \sqrt{< h^2 >}, \quad <h> = \int_{-\infty}^{\infty} h \, p(h) \, \mathrm{d}h = 0, \tag{6}$$

where $p(h)$ is a probability density function and <> denotes spatial averaging over the surface. A height correlation function describes the extent to which information about the height at one point on a surface determines, on average,

the height at another point. In 2D $x_1 x_2$-space, a normalized correlation function $C(r)$ is defined as:

$$C(r) = \frac{< h(x_1)h(x_1 + r) >}{\sigma^2}, \tag{7}$$

where x_1 is the coordinate direction along which the extent of the surface is defined and h is the variation in height from the mean line $x_2 = 0$. The distance between any two points on the surface is denoted by r. Note that $C(0) = 1$ and $C(\infty) = 0$ so that as r increases, $C(r)$ decreases. The correlation length λ_0 is the distance over which $C(r)$ falls to $1/e$. We assume that both the height distribution and the correlation function follow Gaussian distributions, according to the literature [3, 5, 8]:

$$p(h) = \frac{1}{\sigma\sqrt{2\pi}} \exp\left(-\frac{h^2}{2\sigma^2}\right), \quad C(r) = \exp\left(-\frac{r^2}{\lambda_0^2}\right). \tag{8}$$

For the FE simulations, the rough cracks are generated in three stages. Firstly, the discretized upper surface of the crack is obtained from the equations (6) to (8) for specified σ, λ_0 and L. The bottom surface is then generated by applying a spatial filter to the upper surface and the two are then connected. Finally, the crack is translated and rotated to the required location in the model domain.

3.1. Monte Carlo studies of the effect of roughness on tip signal amplitudes

Numerous stochastic studies have been published to investigate the effect of roughness on the reflection of ultrasound by rough crack-like defects and surfaces, for which MC simulations of several hundred realisations were carried out [8, 9, 11, 12]. A similar treatment was adopted here to investigate how increasing the roughness of a defect affects the amplitudes received in a ToFD simulation. An important aspect of MC studies is the convergence of the results, and preliminary analysis indicated that samples of one hundred surfaces were sufficient to gain statistical insight related to the tip diffracted amplitudes. An example is shown in Figure 7(a) for a set of surfaces characterised by the high roughness parameter pair ($\lambda_0 = \lambda_p/2, \sigma = \lambda_p/3$).

The MC amplitude study involved generating six datasets of one hundred rough surfaces characterized by a specified pair (λ_0, σ), with each FE simulation model following the description in Section 2.2 and Figure 4, but with the smooth defect replaced by a rough defect of the same length. A fixed value of correlation length $\lambda_0 = \lambda_p/2 \simeq 0.594$mm (recalling that a centre frequency of 5MHz was used) and two incident angles, $\gamma = 70°$ and $50°$, were investigated for
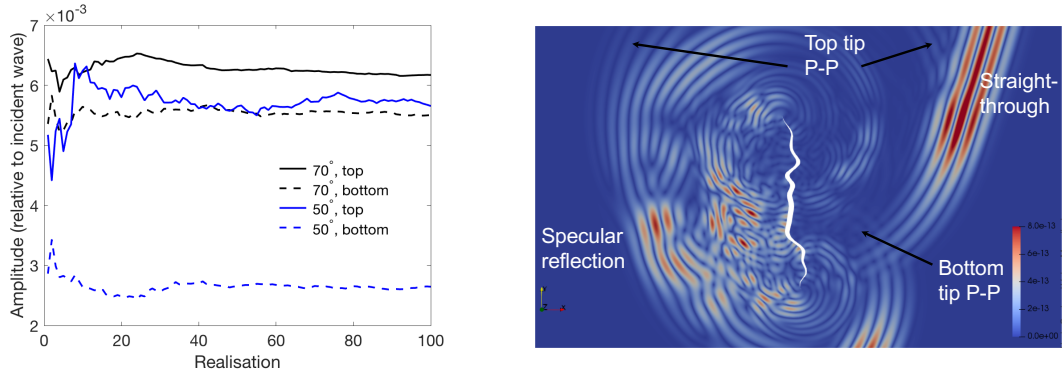
(a) Convergence of amplitudes (relative to incident wave) for 100 realisations.

(b) Scattered response for a single realisation insonified by a 5MHz P-wave with $\gamma = 70°$.

Figure 7: MC analysis of tip diffracted signal amplitudes. Part (a) shows the convergence for 100 realisations for the case of $\lambda_0 = \lambda_p/2, \sigma = \lambda_p/3$ for two incident angles: $\gamma = 50°$ and $70°$. Part (b) illustrates the range of amplitudes and wave modes for the different scattering mechanisms.

six choices of σ:

$$\lambda_p/12 = 0.10\text{mm}, \ \lambda_p/10 = 0.12\text{mm}, \ \lambda_p/8 = 0.15\text{mm}, \ \lambda_p/5 = 0.24\text{mm}, \ \lambda_p/4 = 0.30\text{mm}, \ \lambda_p/3 = 0.40\text{mm}.$$

245   The rationale for the selection of beam angles was to compare an accepted optimal angle $\gamma = 70°$ [14] with a case,

$\gamma = 50°$, from the lower range of possible angles.

A maximum face-to-face separation of 0.2mm was implemented for the embedded defects and the top tip was again located at a depth of 30mm. An illustrative example is shown in Figure 7(b), where several important physical features are visible. The wave demonstrating the largest amplitudes is the straight-through signal, followed by the specular

250   reflection from the left surface. The diffracted signals collected and interpreted for ToFD are those radiating from the two tips, that propagate to the top right corner of Figure 7(b). The first arrivals (P-P mode) are the pale concentric wave fronts emanating from the top tip. Mode converted shear waves (with a visibly smaller wavelength) and surface waves are also apparent, and there are several additional waves resulting from secondary scattering mechanisms.

The first three values of σ, 0.1 to 0.15mm, cover roughness RMS heights consistent with those measured for

255   thermally fatigued and stress corrosion cracks, which typically reach 100 microns [23]. The cases of $\sigma \geq \lambda_p/5$ may be classified as very rough, and of course this roughness grows for smaller values of correlation length (i.e. when the lateral spacing of peaks and troughs is reduced). Therefore, the range of roughness considered here takes into account

both medium-range and extreme cases that may arise in plant.

The results for the six cases are plotted together with the FE amplitude for the smooth defect of the same size in

Figure 8, for both $\gamma = 50°$ and $70°$. The mean amplitude was calculated as the average over the one hundred scattered

amplitudes, each normalised with respect to the incident wave amplitude. As for the smooth defects of Section 2.2,

the means were calculated using the centre frequency component amplitude. The spread of results associated with the

mean amplitudes are shown by the dashed lines which represent ± 1 standard deviation.

(a) Top tip.　　　　　　　　　　　　　　(b) Bottom tip.
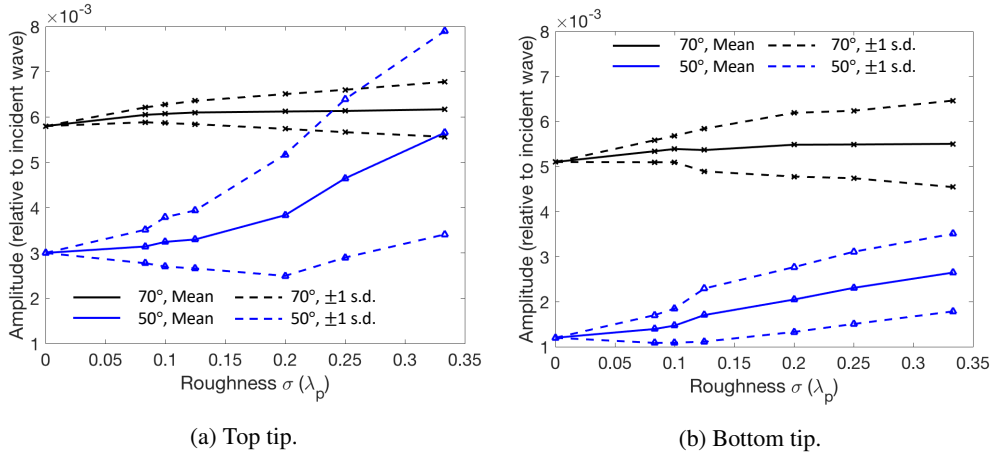
Figure 8: Mean amplitude for six sets of 100 realisations for $\gamma = 70°$ and $50°$, with upper and lower confidence bounds of ± 1 standard deviation shown by dashed lines. Correlation length is $\lambda_0 = \lambda_p/2$ for all cases with σ varied from $\lambda_p/12$ to $\lambda_p/3$. Amplitudes are normalised relative to the incident wave; smooth defect values are plotted for zero roughness.

3.2. Discussion of the results

A primary motivation for the MC study was to clarify whether the rough defect amplitudes are significantly different from those observed for smooth defects of the same size, an important factor when designing inspections for components where rough defects may arise. The smooth defect values, normalised with respect to the incident P-waves, are shown for $\sigma = 0$ in Figures 8(a), for the top tip, and 8(b) for the bottom tip. In the limit as $\sigma \to 0$, the mean amplitudes for the rough defects tend towards the smooth defect values.

Considering that diffracted wave signals are scattered by the tips of a crack-like defect, rather than its surface, the impact of variation of height along its extent on the tip signals is not clear. However, the complexity of elastic wave scattering that encompasses mode conversions and, crucially, surface wave excitations means that roughness is likely to have a direct impact, and this is supported by Figure 8. For $\gamma = 50°$, illustrated by the blue datasets, as roughness

increases from left to right, the top (Figure 8a) and bottom (Figure 8b) tips show significant increases in amplitude, compared with the smooth defect case. In particular, the standard deviation of the amplitude for the top tip signals in Figure 8a increases dramatically at high roughness, implying that certain geometries will produce larger diffraction amplitudes for $\gamma = 50°$ than for $\gamma = 70°$, even though for a smooth defect, the opposite is true by a factor of two. The results for $\gamma = 70°$ indicate much more stability, with even the roughest cases showing relatively little variation from the smooth defect amplitudes for both top and bottom tips.

The effect of beam angle is intrinsically linked with the roughness when analysing the scattering of ultrasonic waves, particularly for smaller values of γ since it influences the proportion of straight-through signal that may be directly reflected by leading facets or peaks on the surface. Another related detail is that the lower the angle, the greater the time difference between top and bottom tip arrivals. This was evident in Figure 2a, where for $\gamma = 70°$, the difference is around $0.7\mu s$. Conversely, for $\gamma = 30°$ in Figure 2b, the spacing is nearly two microseconds for the smooth defect, whilst the rough defect A-scan is inconclusive. The reason this time window is so relevant is that it affords additional time for surface waves, generated at the top tip, to propagate along the defect faces which leads to secondary scattering into bulk and surface waves as peaks and troughs are encountered. The larger the window, the more multiple scattering occurs, and the more convoluted the A-scan, as illustrated by the dashed red curve in Figure 2b.

As γ increases to larger values, such as $70°$ for the black datasets in Figure 8, the top and bottom tip signals both arrive within a very small time window, leaving minimal time for additional scattering signals to arrive between them. Therefore, even with increased roughness, the mean tip amplitudes (both top and bottom) remain stable albeit with increased variability as shown by the dashed lines. In conclusion, the accepted range of $65° − 70°$ appears to also work well for the ToFD inspection of rough defects, although there is greater variation in possible amplitudes as very rough levels are reached. As γ is reduced, the effect of roughness becomes more relevant leading to generally higher amplitudes and significantly more variability, as illustrated for the top tip and $\gamma = 50°$ in Figure 8a.

4. Physical scattering mechanisms associated with beam angle and roughness

Tip signal amplitudes are greatest for beam angles of around $\gamma = 70°$ for P-wave incidence for smooth defects, and the level of these amplitudes remains comparatively high for rough defects as shown in Figure 8. The relatively low spread of results demonstrated by the MC analysis indicates that this is a reliable choice, even for inspections where

300 very rough defects may be expected. This is an encouraging result but the emphasis of a ToFD inspection technique is the capability to separate the top and bottom tip signals in order to size a defect.

Recall Figure 2, where A-scans for a smooth and rough defect of the same size ($L = 6$mm) are shown for two beam angles $\gamma = 70°$ and $30°$ in parts (a) and (b), respectively. The dashed curves denote the rough defect in each case. The results for an optimal angle $\gamma = 70°$ in Figure 2a illustrate that the rough defect signal amplitudes are similar to the

305 smooth defect (solid curve) and that the top and bottom tip signals are sufficiently separated to estimate the size of the defect accurately. In contrast, the A-scan for the same rough defect for $\gamma = 30°$ in Figure 2b shows a leading amplitude five times larger than observed for the smooth defect at the same angle of incidence, and with no discernible bottom tip peak.

Two natural questions arise from this: why should amplitudes increase significantly for some defects at lower values

310 of γ and what reasons lead to the appearance of continuous signals for which it is difficult to separate top and bottom tip arrivals? In this section, explanations of the physical scattering mechanisms for individual cases are provided, which give insight for the interpretation of ToFD signals for rough defects.

Two specific rough surfaces are considered, for the same values of the statistical parameters $\lambda_0 = \lambda_p/2 = 0.594$mm and $\sigma = \lambda_p/4 = 0.297$mm. Case 1 and the associated A-scan for the P-P diffracted waves are shown for $\gamma = 50°$ in Figure 9. The corresponding smooth defect signal is shown in Figure 9(b) by the dot-dashed line, and shows four
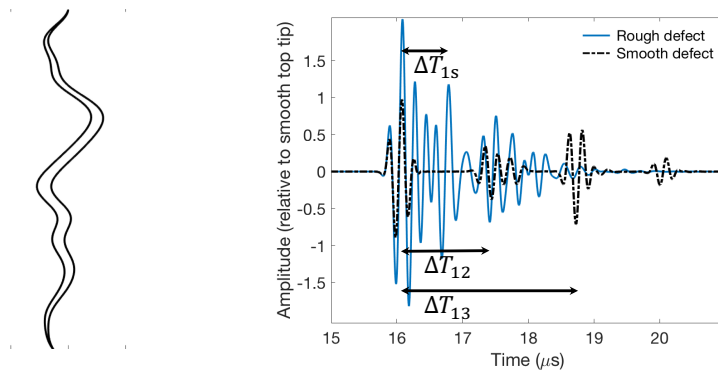
(a) Geometry of 6mm rough defect. (b) A-scans for rough, and corresponding, smooth defect.

Figure 9: Geometry of 6mm defect for case 1 with $\gamma = 50°$ and $\lambda_0 = \lambda_p/2 = 0.594$mm, $\sigma = \lambda_p/4 = 0.297$mm. The diffracted signals for the rough and smooth case are shown in part (b).

315

distinct waveforms. It is notable that the second of these waveforms has a reduced amplitude and small tail; this is a result of interference with the straight-through signal.

Following the calculations of equations (5), the smooth defect time differences are found to be $\Delta T_{12} = 1.30\mu s$ and $\Delta T_{13} = 2.66\mu s$, which are consistent with Figure 9(b). For the rough defect, it is not immediately clear where the bottom tip waveform is within its A-scan signal. Knowledge of its location is indicated by the smooth defect signal in Figure 9(b) and it is apparent that both the top-bottom tip phase change has been diluted, and that the continuous signal makes characterisation difficult. Even more problematic is the appearance of a relatively large peak at $t = 16.8\mu s$, which may potentially be misidentified as a bottom tip signal, leading to an underestimation error in sizing.

The reasons for this misleading peak are linked to secondary scattering effects of an excited surface wave that propagates along the rough defect. Encounters with the rough surface's peaks lead to additional waves being diffracted towards the ToFD receiver, arriving in between the top and true bottom tip signals. Figure 10 illustrates the scattering effects and geometrical considerations. In part (a), the incident wave is shown arriving at the top tip with $\gamma = 50°$.
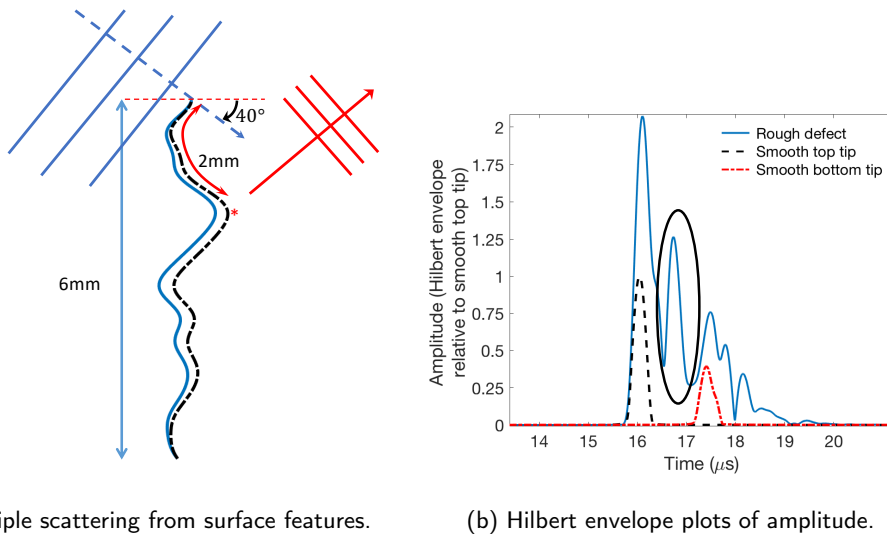
(a) Multiple scattering from surface features.   (b) Hilbert envelope plots of amplitude.

Figure 10: Schematic illustration of scattering mechanisms for $\gamma = 50°$ for case 1. The Hilbert envelopes of the rough defect A-scan, and the top and bottom tip signals for the smooth defect, are shown with the secondary scattered bulk P-wave highlighted by the black ellipse.

The top tip signal peaks in Figure 9(b) and 10(b) show a slight broadening and increase in amplitude compared with the smooth tip waveforms. This is likely to be due to secondary scattering, of the primary tip-diffracted waves, from the surfaces close to the top tip (e.g. regions between the top tip and the peak denoted as ∗) in Figure 10(a). A more prominent feature is the A-scan peak highlighted by the ellipse in Figure 10(b), which results from another diffracted wave radiating from the feature ∗, which is located around a third of the way along the defect in Figure 10(a).

A surface wave, excited at the top tip, traverses the rough surface for approximately 2mm before mode conversion results in a bulk wave being excited and diffracted towards the receiver. Checking the associated time differences, in Figure 9(a), for this peak (ΔT_{1s}) and the bottom tip peak (T_{12}), we find:

$$\Delta T_{1s} = \frac{2\text{mm}}{c_R} = 0.70\mu s; \qquad \Delta T_{12} = 2\frac{L\cos 50°}{c_p} = 1.30\mu s.\qquad (9)$$

Comparison with Figure 10(b) is consistent with these approximate time differences with respect to the top tip signal, noting that the secondary peak occurs close to halfway between the top and bottom tip signals which may lead to underestimation of length by up to 50%.

This insight regarding additional surface wave mode conversions is important when interpreting ToFD A-scans for sizing. A crucial aspect is the length of the defect that surface waves may travel before the bottom tip signal is excited. For example, Figure 10(b) indicates that the bottom tip signal arrives $1.3\mu s$ after the top signal. This time window equates to a distance of $1.3\mu s \times c_R = 3.9$mm, which is just a little before a surface wave may encounter the two bumps in the defect's lower half in Figure 10(a). The small peaks in Figure 10(b) after $17.3\mu s$ occur due to further multiple scattering events.
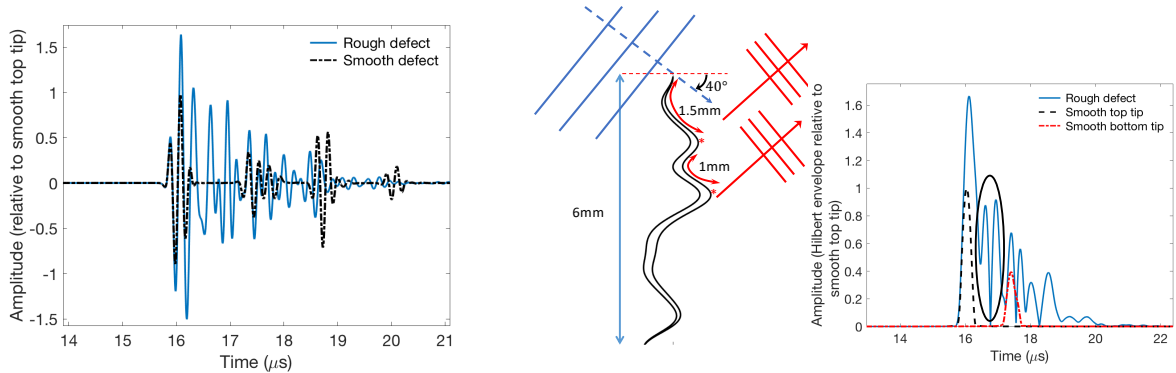
Figure 11: Case 2 for $\lambda_0 = \lambda_p/2 = 0.594$mm and $\sigma = \lambda_p/4 = 0.297$mm. The A-scans, defect geometry ($L = 6$mm) and Hilbert envelope plots of amplitude are shown for $\gamma = 50°$ for the P-P diffracted signals of the rough and smooth case. A black ellipse is used to highlight the additional 2 peaks between the top and bottom tip arrivals.

Case 2 produces a more complicated A-scan, as illustrated in Figure 11. This time, two rough surface peaks produce multiple scattering effects that contribute two amplitude peaks in the Hilbert envelope plot before the bottom tip signal arrives. This observation is explained via the A-scan, schematic diagram and the circled double peak between $t = 16\mu s$ and $17\mu s$ in Figure 11. There are also three further amplitude peaks that arise from multiple scattering of surface waves

as they propagate over the rough surface. This specific example may lead to either a significant underestimation or an inconclusive outcome when conducting a ToFD A-scan inspection.
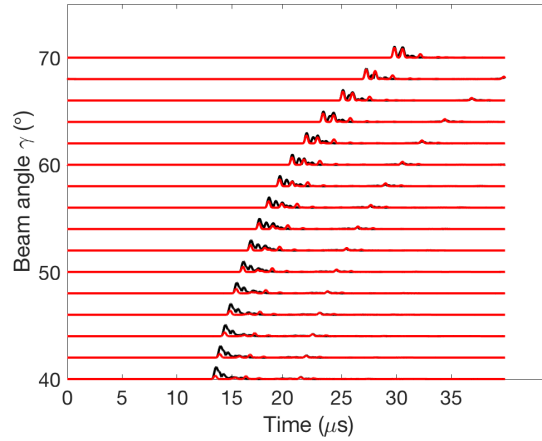
Figure 12: Stacked A-scans for $40° \leq \gamma \leq 70°$ (plotted at 2° intervals) for a rough defect with $\lambda_0 = \lambda_p/2 = 0.594$mm and $\sigma = \lambda_p/4 = 0.297$mm. The rough defect signals are represented by the black curves, and the corresponding smooth defect signals, by the red curves.

It is clear that as σ grows or λ_0 falls, these phenomena will have more effect if the beam angle is insufficiently large; the larger the angle, the smaller the amount of time for surface waves to propagate along the rough surface and be repeatedly scattered. This conclusion is illustrated in Figure 12, where sixteen A-scans for a specific realisation are stacked. Additional misleading peaks may arise for angles up to $\gamma = 65°$. Only at around $\gamma = 70°$, do the peaks of the black curves (the rough defect A-scans) correctly line up with the corresponding smooth defect curves (red) which indicate the true top and bottom tip locations. For $44° \leq \gamma \leq 60°$, the central peak (which would lead to size underestimation if taken as the bottom tip signal) is significantly larger than the true bottom tip amplitudes.

5. Sizing rough defects using ToFD

Crack sizing using ToFD is critical in NDE as the length of a crack significantly affects the structural integrity of the engineering component. As shown in preceding examples such as Figure 10, when the crack is smooth, two clear tip diffraction signals can be identified and the time interval between them may be precisely determined. In contrast, for a rough crack, tip-diffracted waves may be masked by the additional scattered waves from the rough surface, causing significant uncertainties when sizing the crack length. In this section, the methodology of crack sizing is introduced and the impact of crack surface roughness, upon accuracy of ToFD sizing results, is discussed using statistical analysis.

5.1. Crack sizing methods

The scattered signals from the MC simulations in Section 3.1 are post-processed here to determine the rough crack length. Two different techniques (i.e. auto-correlation function and envelope peak detection) are implemented to calculate the difference in arrival times of the top and bottom tip diffraction signals, and then the defect size is obtained by considering simple geometrical ray paths. The auto-correlation function (ACF) method is often used in signal processing to analyse time domain signals and involves correlating a signal with a delayed copy of itself. One common application is to identify special features or repeating patterns, that are otherwise obscured by noise. The ACF of a real scattered signal $f(t)$ may be defined as:

$$\mathrm{ACF}\,(\tau) = \int_{-\infty}^{\infty} f(t+\tau) f(t) \, \mathrm{d}t \tag{10}$$

where t is a dummy variable and τ represents the time lag.

Figure 13a depicts the normalized auto-correlation function (NACF) of the ToFD signal for one realisation from Section 3.1 (low roughness, $\sigma = \lambda_{\mathrm{p}}/12$). The auto-correlation function is normalized using its value at zero time lag (i.e. $\mathrm{NACF}(\tau) = \mathrm{ACF}(\tau)/\mathrm{ACF}(0)$). For a smooth or a slightly rough defect, the NACF shows two main pulses (enclosed by the rectangular dashed boxes in Figure 13a); the first pulse at zero time lag refers to the signal completely overlapping with itself, and the second pulse with a smaller amplitude arises when the top tip signal overlaps with the bottom tip signal. The difference in times of arrival, ΔT_{tb}, is determined by estimating the time lag between the largest peaks in the two pulses. Furthermore, since the top and the bottom signals have a phase change of around π, the absolute value of NACF is used to find ΔT_{tb}.

It is also worth noting that due to the finite bandwidth of the signal, there are multiple large peaks around zero time lag in Figure 13a (highlighted by the dashed black box). A threshold is introduced here to help select the correct second pulse. Specifically, the peaks with a time lag smaller than one period (i.e. $|\tau| \leq \frac{3\lambda_{\mathrm{p}}}{c_{\mathrm{p}}} = 0.6\mu s$) are not considered while detecting the largest peak in the second pulse.

An alternative way to find ΔT_{tb} is to extract it from the signal envelope constructed using the Hilbert transform. As shown in Figure 13b, in an ideal case ΔT_{tb} can be identified as the time interval between the peak of the first arrival and the peak of the second largest envelope arrival. The first arrival corresponds to the top tip diffraction signal and

(a) NACF
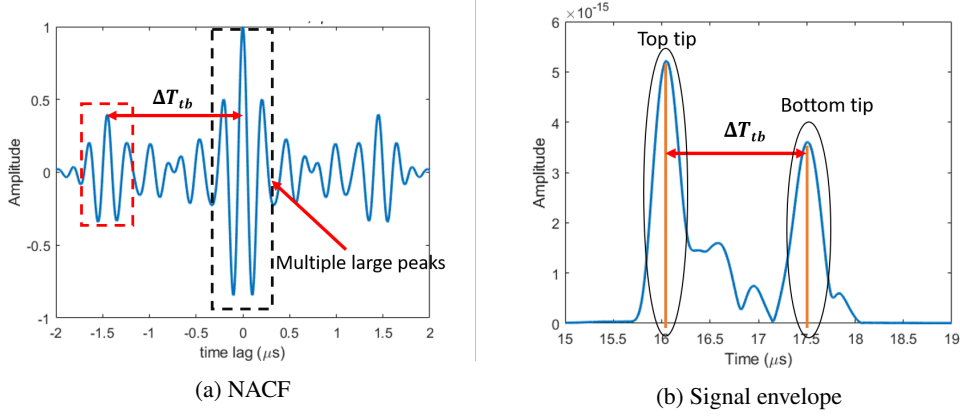
(b) Signal envelope

Figure 13: The NACF (a) and signal envelope (b) methods for determining the difference in arrival times for the top and bottom tip-diffracted signals for a low roughness case with $\sigma = \lambda_p/12$ for $\gamma = 50°$.

the second largest one represents the bottom tip diffraction signal. However, surface roughness can significantly distort the waveform via several distinct peaks caused by additional scattering events. In some cases the additional scattered waves may be significant and it becomes very challenging to identify the correct bottom tip signal for sizing, e.g. Figure 10(b). A threshold, similar to that applied to the ACF, is used so that the time interval between selected peaks must be larger than one period of the signal (i.e. $0.6\mu s$).

Once ΔT_{tb} has been acquired, the defect length L can be easily calculated according to the basic geometric relationships illustrated in Figure 4a. The wave paths of the two tip diffracted waves are indicated by the distances labelled as R and R_b in Figure 4a, with the total distances travelled equal to $2R$ and $2R_b$, respectively. Denoting the horizontal distance between the transducers as $2w = 2d \tan \gamma$, the difference of the two wave paths for the P-P mode, ΔD_p can be expressed as:

$$\Delta D_p = 2 \left(\sqrt{w^2 + (d + L)^2} - \sqrt{w^2 + d^2} \right) = c_p \Delta T_{tb} . \tag{11}$$

After rearranging, and using some trigonometric simplification, the theoretical crack length can be calculated as a function of d and γ only, given c_p and ΔT_{tb}:

$$L = \sqrt{\left(\frac{d}{\cos \gamma} + \frac{c_p \Delta T_{tb}}{2} \right)^2 - d^2 \tan^2 \gamma} - d . \tag{12}$$

5.2. Sizing results and discussion for rough defects

Figure 14 illustrates the ToFD sizing results obtained from both the auto-correlation function and envelope peak detection approaches for all the cases considered in the MC analysis of Section 3.1. Perhaps the most interesting aspect of the results is that when the incident angle is $\gamma = 70°$, the sizing results are very accurate and the surface roughness appears to have little impact on the accuracy of sizing. In addition, the estimated defect length approximately follows a normal distribution, regardless of the roughness. On the contrary, when γ decreases to 50°, large errors are observed, especially when the surface roughness exceeds $\lambda_p/10$, and this may result in significant underestimation of the defect length. The distribution of crack lengths also no longer follows a normal distribution once σ exceeds $\lambda_p/10$ for the lower value of γ.


(a) incidence angle: 70°   (b) incidence angle: 50°
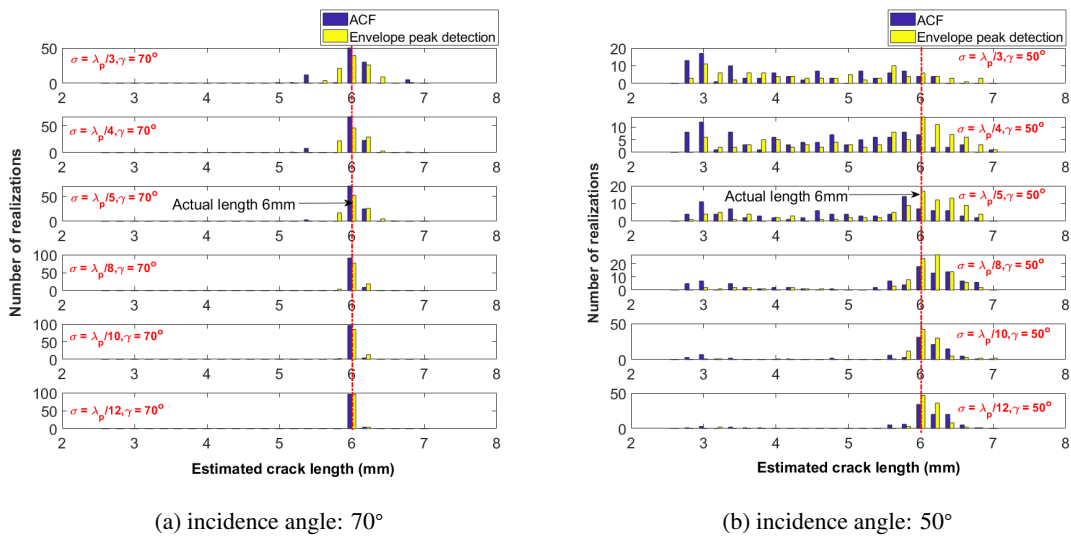
Figure 14: Rough crack ToFD sizing results using both auto-correlation function and envelope peak detection methods. Incident angles (a) $\gamma = 70°$ and (b) $\gamma = 50°$. The actual length of cracks is 6mm.

Figure 15 summarises the results of Figure 14 by showing the mean value, and the associated error bars, of the sizing results for the crack length. It is worth noting that the spread of error bar is ± 1 standard deviation which is consistent with Figure 8. The mean value is very close to the true length when $\gamma = 70°$ in Figure 15a, and the error bars for the highest roughness value are only 0.3mm for the ACF method and 0.2mm for the envelope peak detection method, indicating a maximum sizing error of around 6% and 3% respectively.

However when $\gamma = 50°$, the mean value clearly decreases as the roughness becomes larger, showing severe underestimation of the defect length. In addition, the error bars become very large, reaching almost 1.2mm (ACF method)
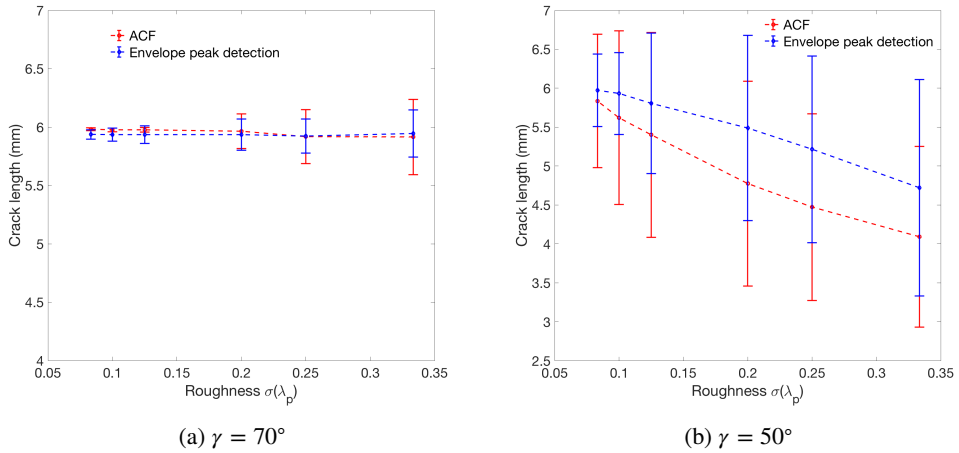
(a) $\gamma = 70°$ (b) $\gamma = 50°$

Figure 15: The mean value and error bars (± 1 standard deviation) for rough crack sizing results with incident angle (a) $\gamma = 70°$, (b) $\gamma = 50°$. The actual length of cracks is 6mm.

and 1.3mm (envelope peak detection method) when $\sigma = \lambda_p/3$ and the maximum sizing error may be as large as 50%. Therefore, to achieve accurate sizing results with smaller uncertainty, 70° is a statistically optimal choice.

It may also be noticed that for $\gamma = 70°$ and low values of roughness (i.e. $\sigma < \lambda_p/5$), the ACF method is slightly more accurate than the envelope peak detection method. This can be explained by the fact that even low surface roughness can distort the shapes of the tip signal envelopes, so that their peaks will slightly shift, leading to errors in crack sizing. In contrast, auto-correlation can average out small incoherent noise caused by low roughness, and hence enhance the coherent part of the signal. Overall though, the two methods are both accurate when $\gamma = 70°$.

In practice, it is not always possible to achieve an inspection angle as large as 70°, due to the geometrical limitation of an engineering component. A reduced inspection angle to a mid-range value such as $\gamma = 50°$, becomes an alternative but it may lead to significant errors and large uncertainties. Figures 16a-16c illustrate why both the ToFD sizing methods implemented here, are more likely to undersize rough defects.

Section 4 explains how surface roughness may induce additional scattered waves (e.g. those converted from Rayleigh waves), which arrive at the receiver before the bottom tip signal, as indicated in Figure 16a by the red ellipse. For the envelope peak detection approach shown in Figure 16b, the additional peak that arrives between the top and bottom signals, may be larger than the bottom tip signal, and it is very easy to then underestimate ΔT_{tb} by selecting the erroneous envelope peak. For the ACF method, shown in Figure 16c, the additional scattered waves may induce a large pulse at around -0.7μs, closer to the main pulse at zero lag than the actual bottom signal at around -1.5μs. Hence
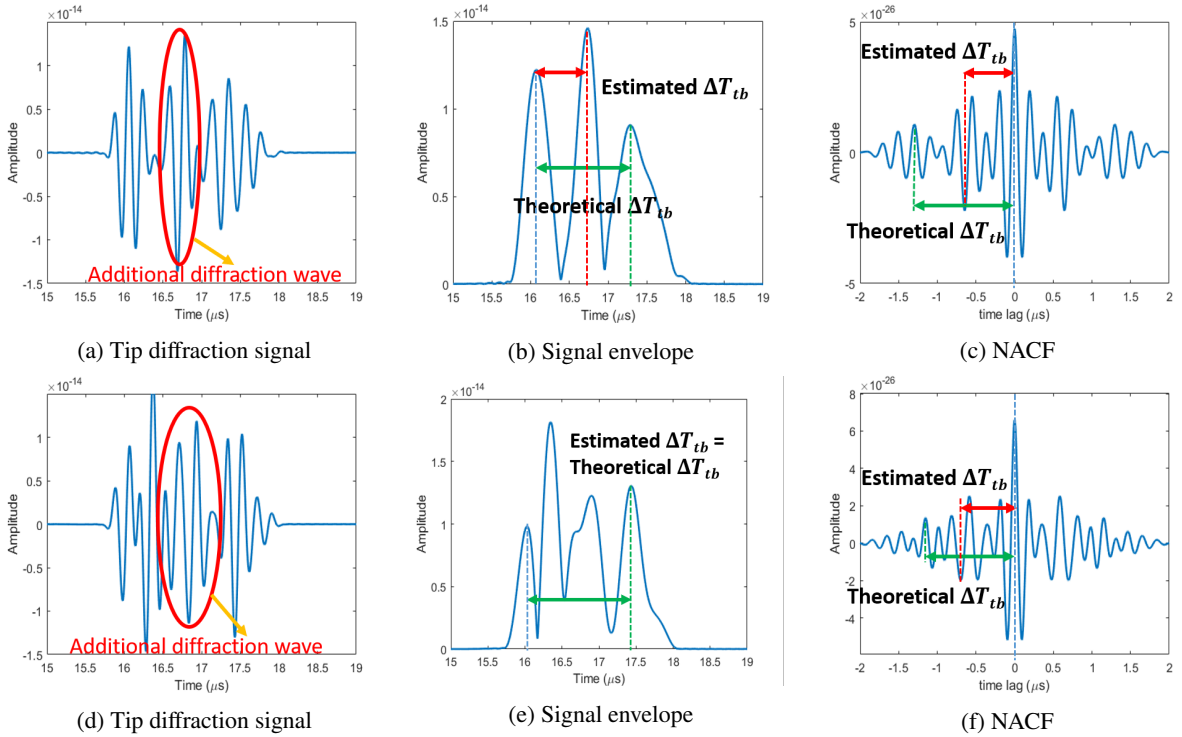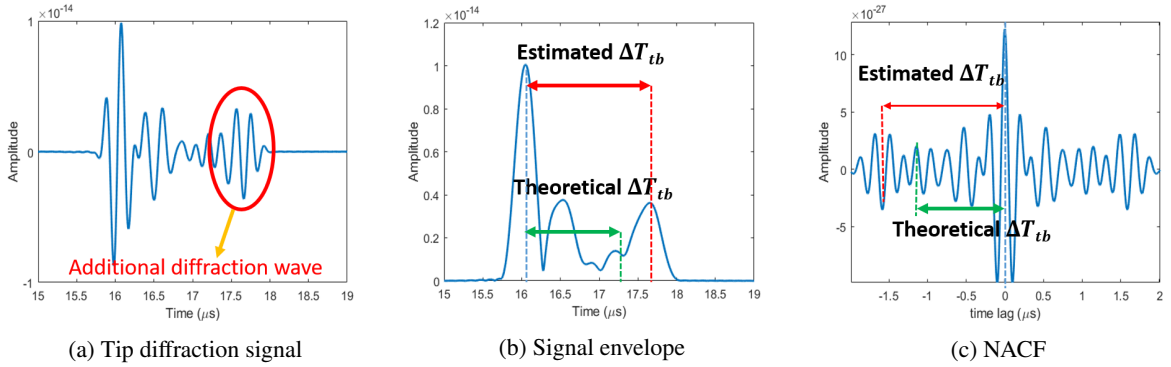
Figure 16: Time-domain tip diffraction signals for examples of cases that underestimate rough crack length. The RMS roughness is $\sigma = \lambda_{\mathrm{p}}/3$.

the ACF approach also tends to undersize the defect.

Although both methods result in considerable sizing uncertainties for $\gamma = 50°$, the envelope peak detection approach seems to produce smaller errors than the ACF approach as shown in Figure 15b. The mean value estimated from the signal envelopes is closer to the true value than the ACF method. Some explanation for this may be provided by a specific example shown in Figures 16d to 16f. As can be seen, when the additional scattered wave amplitudes are not excessively large, the envelope peak detection approach may still locate the correct timing of the bottom signal in Figure 16(e), and therefore ΔT_{tb} is correctly estimated. However, with ACF the additional pulse is sufficiently significant to lead to underestimation of ΔT_{tb} and the defect size.

It should also be noted that although it is more likely for underestimation to occur, there are also cases when the length is overestimated, as shown in Figure 17. A clear wave tail can be seen (highlighted by the red circle in Figure 17a), which arrives later than the bottom tip signal, but its amplitude is large. This will again lead to the misidentification of the bottom signal, causing an oversizing of the defect as illustrated in Figure 17b and 17c. The long tail can be attributed to multiple scattering effects or bulk waves diffracted from mode conversion of Rayleigh

(a) Tip diffraction signal   (b) Signal envelope   (c) NACF

Figure 17: Time-domain tip diffraction signals for overestimation of rough crack length. The RMS roughness is $\sigma = \lambda_{\mathrm{p}}/3$.

waves, as explained in Section 4.

6. Conclusions

Ultrasonic ToFD techniques are widely used, and highly effective, for detecting and sizing crack-like defects. Once a crack has been located, a pair of transmitting and receiving transducers may be positioned symmetrically either side of the defect, in order to size it by evaluating the difference in top and bottom tip arrival times. This procedure becomes more difficult for rough defects, for which amplitudes and waveforms show significant variation when compared with smooth defects of the same size.

Although it has been shown that incident beam angles identified as optimal for P waves for smooth defects prove to also be effective for rough defects, there is significant variability as roughness increases. In particular, for beam angles even only slightly reduced, amplitudes are shown to increase and A-scan signals become increasingly challenging to interpret for sizing capability. The physical scattering mechanisms that lead to continuous signals have been explained, with the reduction in beam angle allowing more propagation time for surface waves to traverse the rough surface. This increased interaction time leads to more multiple scattering of diffracted bulk waves as the surface waves encounter peaks and troughs. The additional scattering and interference effects increase the uncertainty of sizing and contribute A-scan features that may be misidentified as a bottom tip signal, leading to underestimation of defect extent.

Two methods (autocorrelation and envelope peak detection) are used to estimate the difference in arrival times of top and bottom tip signals, and the crack length may then be determined. The statistical sizing results are consistent with the observations that the surface roughness induces uncertainties associated with crack sizing. It is notable that

for $\gamma = 70°$, the sizing results are reasonably accurate, because two tip signals can be clearly identified. As the incident angle is reduced to 50°, the MC analysis demonstrates that the majority of estimated crack lengths are lower than the true length, and this trend becomes more apparent as the roughness increases. The additional scattered waves associated with increased roughness and multiple scattering effects, arrive at the receiver earlier than the bottom signal; the bottom signal is weak and sometimes can be masked by these multiple scattering waves. The underestimation of defect length is mainly caused by erroneously selecting the false tip signals. It is also found that at 50°, the errors of sizing are slightly smaller for the envelope peak detection method than when using the ACF approach.

The numerical studies in this article have assumed a constant value of the correlation length, namely half the incident wavelength. The motivation for this choice was its practical value as discussed in previous literature [9, 11] but it would be very interesting to investigate the effects of varying correlation length in the future. Furthermore, the current study focuses only on the P-P diffracted waves, and it would also be very useful to investigate other combinations of modes (e.g. S-S, P-S and S-P), particularly for shear wave incidence. An additional desirable investigation will be the fully three-dimensional FE simulation and experimental work, using the results of this comprehensive two-dimensional study, to gain further important insights.

7. Acknowledgements

References

[1] J. A. Ogilvy, Theory of wave scattering from random rough surfaces, CRC Press, 1991.

[2] J. A. Ogilvy, Theoretical comparison of ultrasonic signal amplitudes from smooth and rough defects, NDT & E International 19 (1986) 371–385.

[3] J. A. Ogilvy, Computer simulation of acoustic wave scattering from rough surfaces, Journal of Physics D: Applied Physics 21 (2) (1988) 260–277.

[4] J. A. Ogilvy, I. D. Culverwell, Elastic model for simulating ultrasonic inspection of smooth and rough defects, Ultrasonics 29 (6) (1991) 490–496.

[5] E. I. Thorsos, The validity of the Kirchhoff approximation for rough surface scattering using a Gaussian roughness spectrum, The Journal of the Acoustical Society of America 83 (1) (1988) 78–92.

[6] J. R. Pettit, A. E. Walker, M. J. S. Lowe, Improved detection of rough defects for ultrasonic nondestructive evaluation inspections based on finite element modeling of elastic wave scattering, IEEE Transactions on Ultrasonics, Ferroelectrics, and Frequency Control 62 (10) (2015) 1797–1808.

[7] J. Zhang, B. W. Drinkwater, P. D. Wilcox, Longitudinal wave scattering from rough crack-like defects, IEEE Transactions on Ultrasonics, Ferroelectrics, and Frequency Control 58 (10) (2011) 2171–2180.

[8] J. Zhang, B. W. Drinkwater, P. D. Wilcox, Effect of roughness on imaging and sizing rough crack-like defects using ultrasonic arrays, IEEE Transactions on Ultrasonics, Ferroelectrics, and Frequency Control 59 (5) (2012) 939–948.

[9] F. Shi, M. J. S. Lowe, X. Xi, R. V. Craster, Diffuse scattered field of elastic waves from randomly rough surfaces using an analytical Kirchhoff theory, Journal of the Mechanics and Physics of Solids 92 (2016) 260–277.

[10] F. Shi, M. J. S. Lowe, R. V. Craster, Diffusely scattered and transmitted elastic waves by random rough solid-solid interfaces using an elasto-dynamic Kirchhoff approximation, Physical Review B 95 (21) (2017) 214305.

[11] S. G. Haslinger, M. J. S. Lowe, P. Huthwaite, R. V. Craster, F. Shi, Elastic shear wave scattering by randomly rough surfaces, Journal of the Mechanics and Physics of Solids 137 (2020) 103852.

[12] S. G. Haslinger, M. J. S. Lowe, R. V. Craster, P. Huthwaite, F. Shi, Prediction of reflection amplitudes for ultrasonic inspection of rough planar defects, Insight 63 (1) (2021) 23–28.

[13] Non-destructive testing – ultrasonic testing – time-of-flight diffraction technique as a method for detection and sizing of discontinuities (BS EN ISO 16828:2014), British standards institution (2014).

[14] J. A. Ogilvy, J. A. G. Temple, Diffraction of elastic waves by cracks: application to time-of-flight inspection, Ultrasonics 21 (1983) 30–40.

[15] R. K. Chapman, J. M. Coffey, A theoretical model of ultrasonic examination of smooth flat cracks, in: Review of Progress in Quantitative Nondestructive Evaluation, Springer, 1984, pp. 151–162.

[16] J. B. Keller, Geometrical theory of diffraction, JOSA 52 (2) (1962) 116–130.

[17] A.-W. Maue, Die Beugung elastischer Wellen an der Halbebene, ZAMM-Journal of Applied Mathematics and Mechanics/Zeitschrift für Angewandte Mathematik und Mechanik 33 (1-2) (1953) 1–10.

[18] J. D. Achenbach, A. K. Gautesen, H. McMaken, Ray methods for waves in elastic solids: with applications to scattering by cracks, Pitman advanced publishing program, 1982.

[19] R. A. Phillips, Efficient numerical modelling of the ultrasonic scattering from complex surface-breaking defects, Ph.D. thesis, Imperial College London (2018).

[20] R. A. Phillips, D. J. Duxbury, P. Huthwaite, M. J. S. Lowe, Simulating the ultrasonic scattering from complex surface-breaking defects with a three-dimensional hybrid model, NDT & E International 97 (2018) 32–41.

[21] M. Kemppainen, I. Virkkunen, Crack characteristics and their importance to NDE, Journal of Nondestructive Evaluation 30 (3) (2011) 143–

157.

[22] J. A. Ogilvy, Model for the ultrasonic inspection of rough defects, Ultrasonics 27 (2) (1989) 69–79.

[23] J. B. Elliott, M. J. S. Lowe, P. Huthwaite, R. A. Phillips, D. J. Duxbury, Sizing subwavelength defects with ultrasonic imagery: An assessment of super-resolution imaging on simulated rough defects, IEEE Transactions on Ultrasonics, Ferroelectrics, and Frequency Control 66 (10) (2019) 1634–1648.

[24] J. D. Achenbach, Wave Propagation in Elastic Solids, North-Holland Publishing Company/American Elsevier, 1973.

[25] P. Huthwaite, Accelerated finite element elastodynamic simulations using the GPU, Journal of Computational Physics 257 (2014) 687–707.

[26] S. G. Haslinger, M. J. S. Lowe, P. Huthwaite, R. V. Craster, F. Shi, Appraising Kirchhoff approximation theory for the scattering of elastic shear waves by randomly rough defects, Journal of Sound and Vibration 460 (2019) 114872.

[27] M. B. Drozdz, Efficient finite element modelling of ultrasound waves in elastic media, Ph.D. thesis, Imperial College London (2008).